Bjoern F. Klose
First *Last*

ASME Paper Title: A Numerical Test Rig for Turbomachinery Flows Based on Large Eddy Simulations With a High-Order Discontinuous Galerkin Scheme - Part II: Shock Capturing and Transonic Flows

Authors: B. F. Klose, C. Morsbach, M. Bergmann, A. Hergt, J. Klinner, S. Grund, E. Kügeler

ASME Journal Title: Journal of Turbomachinery

Volume/Issue 146/2 Date of Publication (VOR* Online) 13. Nov. 2023

ASME Digital Collection URL: https://asmedigitalcollection.asme.org/turbomachinery/article/146/2/021006/116943 Test-Rig-for-Turbomachinery-Flows

DOI: 10.1115/1.4063827

*VOR (version of record)

Bjoern F. Klose[1]
Institute of Test and Simulation for Gas Turbines,
German Aerospace Center (DLR),
Linder Höhe, 51147 Cologne, Germany
email: bjoern.klose@dlr.de

Christian Morsbach
Institute of Propulsion Technology,
German Aerospace Center (DLR),
Linder Höhe, 51147 Cologne, Germany

Michael Bergmann
Institute of Propulsion Technology,
German Aerospace Center (DLR),
Linder Höhe, 51147 Cologne, Germany

Alexander Hergt
Institute of Propulsion Technology,
German Aerospace Center (DLR),
Linder Höhe, 51147 Cologne, Germany

Joachim Klinner
Institute of Propulsion Technology,
German Aerospace Center (DLR),
Linder Höhe, 51147 Cologne, Germany

Sebastian Grund
Institute of Propulsion Technology,
German Aerospace Center (DLR),
Linder Höhe, 51147 Cologne, Germany

Edmund Kügeler
Institute of Propulsion Technology,
German Aerospace Center (DLR),
Linder Höhe, 51147 Cologne, Germany

A Numerical Test Rig for Turbomachinery Flows Based on Large Eddy Simulations With a High-Order Discontinuous Galerkin Scheme - Part 2: Shock-Capturing and Transonic Flows

In the second paper of this three part series, we focus on the simulation of transonic test cases for turbomachinery applications using a high-order discontinuous Galerkin spectral element method (DGSEM). High-fidelity simulations of transonic compressors and turbines are particularly challenging, as they typically occur at high Reynolds number and require additional treatment to reliably capture the shock waves characterizing such flows. A recently developed finite-volume subcell shock capturing scheme tailored for the DGSEM is applied and evaluated with regard to the shock sensor. To this end, we conduct implicit large-eddy simulations of a high-pressure turbine cascade from public literature and a transonic compressor cascade measured at the German Aerospace Center, both at a high Reynolds number above 10^6*. Based on the results, we examine modal-energy and flow-feature based shock indicator functions, compare the simulation data to experimental and numerical studies and present an analysis of the unsteady features of the flows.*

Keywords: large eddy simulation, discontinuous Galerkin spectral element method, transonic flow, shock capturing

1 Introduction

With the increasing demand for more efficient turbo engines, the focus of computational fluid dynamics (CFD) for turbomachinery applications is shifting towards higher fidelity tools, not only for the validation of lower cost methods, but as a valuable complement to experimental campaigns. While such flows are typically at high Reynolds numbers and possibly transonic, the increase in computational resources in recent years and development of sophisticated numerical methods now allows for the simulations of flows under such operating conditions using large-eddy simulations (LES) or even direct numerical simulations (DNS) [1].

There are a number of transonic high-fidelity simulations available in literature - in large part high-pressure turbines (HPT) such as the VKI-LS89. Notable contributions include the first DNS of an HPT by Wheeler *et al*. [2], who analyzed the influence of free-stream turbulent structures on the boundary layer dynamics and heat transfer, as well as the study by Pichler *et al*. [3] on the effect of inlet turbulence through variations in intensity and length scale. Garai *et al*. [4] used a discontinuous Galerkin spectral element method (DGSEM) at very high order to determine the transition mechanism on an HPT and Segui *et al*. [5] were able to closely match the challenging MUR235 [6] operating point through highly resolved LES. More recently, Dupuy *et al*. [7] performed an extensive analysis on the production of intermittent turbulent spots and Zhao *et al*. examine the bypass transition on an HPT [8] and the effect of turbulence generated by upstream bars [9]. For a transonic compressor blade at realistic operating condition, Bode *et al*. [10] analyzed the interaction of free-stream turbulence with the shock through highly resolved LES.

Among the numerical methods used for these high-fidelity computations, high-order spectral methods have become a popular choice over the last few years [1], as they feature reduced dispersion and dissipation errors over lower-order schemes [11, 12] and hence require fewer grid points for a given error margin. The discontinuous Galerkin spectral element method, in particular, has seen a number of recent developments that improve the numerical robustness and accuracy of the method [13–15] and has been proven to perform well in turbomachinery applications [16]. The simulation of transonic flows using high-order methods, however, raises the issue of capturing and resolving local discontinuities at shock fronts and avoiding the associated spurious polynomial oscillations. There is a variety of approaches tailored for spectral element methods to combat the Gibb's oscillations, including artificial viscosity [17–19], finite-volume (FV) subcells [20–23] and filtering [24]. The FV subcell approach has several advantages as it does not require the modification of the underlying differential equations and can be seamlessly blended with the split-forms of

[1]Corresponding Author.
Version 1.18, September 24, 2023

the DG approximation while retaining the entropy stability property with the proper choice of two-point fluxes [21]. Klose *et al.* [25] tested the FV subcell approach on a transonic turbine cascade and found it to perform well in comparison with artificial viscosity. But given that this family of shock-capturing schemes has only been developed recently, simulations of three-dimensional large-scale problems are still scarce.

In this paper, we present results from LES of two transonic turbomachinery cascades: the high-pressure turbine cascade VKI-LS89 and a compressor cascade measured at the German Aerospace Center (DLR). The flows are simulated using a compressible high-order accurate DGSEM, where the FV subcell shock capturing scheme by Hennemann *et al.* [21] is applied for numerical stabilisation and reduction of spurious oscillations.

For the VKI-LS89 turbine cascade, which is simulated at the MUR235 condition [6] with a Reynolds number of 1.17×10^6, high inflow turbulence levels and outflow Mach number of 0.93, we evaluate the default modal oscillation sensor [17, 21] on a structured grid. This HPT test case has been the subject of several publications and is hence a well-suited test case for the DGSEM code, where we compare the LES results to published experimental and numerical campaigns and provide an analysis of the unsteady flow features. For the LES of the transonic compressor cascade at off-design condition, described by Klinner *et al.* [26], we test the default shock sensor, a modification, and a sensor based on flow features [27] on an unstructured, locally refined grid and show the effect they have on the shock resolution and turbulent fluctuations, given that the blending locally increases dissipation. An analysis of the unsteady flow features pertaining to vortex shedding and shock movement is provided subsequently.

2 Numerical method

All simulations in the present work are conducted with DLR's compressible flow solver for turbomachinery applications TRACE with a discontinuous Galerkin spectral element method for the spatial discretization. We employ the nodal collocation approach, where the interpolation and quadrature points are both taken to be the Legendre-Gauss-Lobatto nodes and yield an efficient numerical scheme with diagonal mass matrix [28]. The implicit (no-model) LES approach is chosen for the modelling of subgrid stresses, i.e. dissipation is added implicitly via the numerical dissipation of the Riemann solver. Numerical errors arising from the non-linearity of the advective fluxes and the limited precision of integration are addressed by employing kinetic-energy or entropy conserving split-form approximations of the inviscid fluxes [14, 15], while the Bassy-Rebay-1 (BR1) scheme [29] is applied for the viscous part. An explicit third-order Runge-Kutta scheme is used for the integration of the system of equations in time. For more details on the numerical scheme, we refer the interested reader to the first part of this paper series and to Bergmann *et al.* [30, 31].

2.1 Shock capturing. To reduce unphysical oscillations across shock fronts, the FV subcell shock capturing method by Hennemann *et al.* [21] is applied in elements subject to shock waves and locally blends the high-order operator with a first-order FV scheme:

$$\frac{\partial \mathbf{q}}{\partial t} + \alpha \mathbf{R}^{\mathrm{FV}}(\mathbf{q}) + (1-\alpha)\mathbf{R}^{\mathrm{DG}}(\mathbf{q}) = 0. \tag{1}$$

Here, $\mathbf{R}$ is the inviscid residual operator, $\mathbf{q}$ is the vector of conserved variables and $\alpha \in [0,1]$ is the blending factor based on a shock indicator function.

The semi-discrete low-order FV approximation of the conservation law on the subcell grid is given as

$$J_i \frac{\partial \mathbf{q}_i}{\partial t} + \frac{1}{w_i}\left[\tilde{\mathbf{F}}^*_{i,i+1} - \tilde{\mathbf{F}}^*_{i-1,i}\right] = 0, \tag{2}$$

with the nodal values $\mathbf{q}_i$ representing the mean values within the cells and $\tilde{\mathbf{F}}^*_{i,i+1} = \tilde{\mathbf{F}}^*(\mathbf{q}_i, \mathbf{q}_{i+1})$ the interface flux between the subcells i and $i+1$. For further details on the properties and the implementation of the DG-FV blending scheme, we refer to the paper by Hennemann *et al.* [21].

Two shock indicator functions are employed in this paper: the modal oscillation indicator by Persson & Peraire [17] (and modified by Hennemann *et al.* [21]), and the feature-based indicator by Fernandez *et al.* [27]. The modal oscillation indicator relates the energy contained in the highest two modes of the polynomial to its total energy:

$$\mathbb{E} = \max\left(\frac{m_N^2}{\sum_{j=0}^{N} m_j^2}, \frac{m_{N-1}^2}{\sum_{j=0}^{N-1} m_j^2}\right). \tag{3}$$

Here, m_j are the modal coefficients of the polynomial with the indicator variable chosen to be the product of pressure and density $p \cdot \rho$. The blending weight is then defined as a function of the energy indicator, $\alpha = f(\mathbb{E}, N) \in [0,1]$, where we set f to either be non-linear mapping function according to [21] (*default*),

$$\alpha = \left(1 + \exp\left(\frac{-s_\alpha}{\mathbb{T}}(\mathbb{E} - \mathbb{T})\right)\right)^{-1}, \tag{4}$$

with $s_\alpha \approx 9.21$ or a linear mapping function

$$\alpha = 0.5 \cdot \frac{\mathbb{E}}{\mathbb{T}}. \tag{5}$$

The threshold $\mathbb{T}$ is calculated following the relation given in [21] as $\mathbb{T}(N) = 0.5 \cdot 10^{-1.8(N+1)^{1/4}}$, unless specified otherwise.

For the feature-based indicator by Fernandez *et al.* [27], we compute the shock sensor $\mathbb{S}$ as the product of a dilatation sensor s_θ and the Ducros vorticity sensor s_ω:

$$\mathbb{S} = s_\theta \cdot s_\omega, \tag{6}$$

$$s_\theta = -\frac{h_\beta}{N}\frac{\nabla\cdot\mathbf{v}}{a^{\mathrm{sonic}}}, \tag{7}$$

$$s_\omega = \frac{(\nabla\cdot\mathbf{v})^2}{(\nabla\cdot\mathbf{v})^2 + \|\nabla\times\mathbf{v}\|_2 + \varepsilon}, \tag{8}$$

$$h_\beta = \frac{\|\nabla\rho\|_2}{(\nabla\rho^{\mathrm{T}}\mathbf{M}_h^{-1}\nabla\rho + \varepsilon)^{1/2}}. \tag{9}$$

Here, a^{sonic} is the speed of sound at sonic conditions, $\varepsilon \ll 1$ is a small number to avoid division by zero, $\|\cdot\|_2$ refers to the L^2 norm and $\mathbf{M}_h$ are the metric terms of the element such that h_β is the local element size along the density gradient. An element-wise constant blending factor is computed from the arithmetic mean of the element-wise maximum and average values and the indicator is mapped linearly onto the unit interval according to Eq. (4) or (5), with $\mathbb{E} = (\max(\mathbb{S}) + V^{-1}\int_V \mathbb{S}\,dV)/2$. Following physical arguments [27], the threshold for the feature-based sensor is set to $\mathbb{T} = 2/(\gamma^2 - 1)^{0.5}$. However, we have found it necessary to scale the threshold by 0.1 to add adequate diffusion to elements containing shocks.

The element-wise constant blending weights resulting from the shock indicator functions are diffused through spatial relaxation between adjacent elements to avoid large jumps in the accuracy of the spatial discretization. Additionally, a time relaxation can be added to avoid sudden changes of the sensor between time steps. In this work, we limit the blending weight to $\alpha_{\max} = 0.5$ for all simulations to restrict the added numerical diffusion from the FV subcells and limit jumps in spatial accuracy between elements.

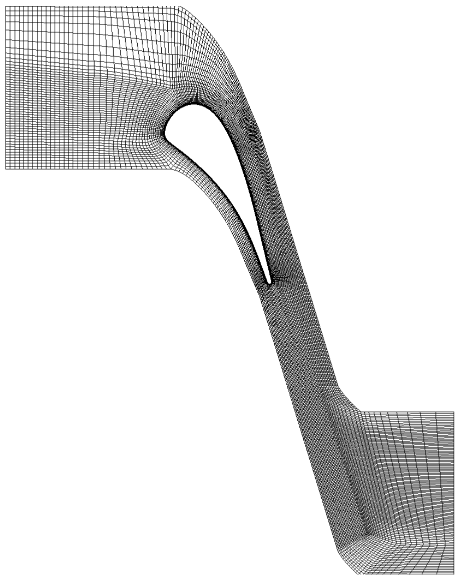

Fig. 1 Computational grid for the high-pressure turbine cascade VKI-LS89. Only elements without interior collocation points shown.

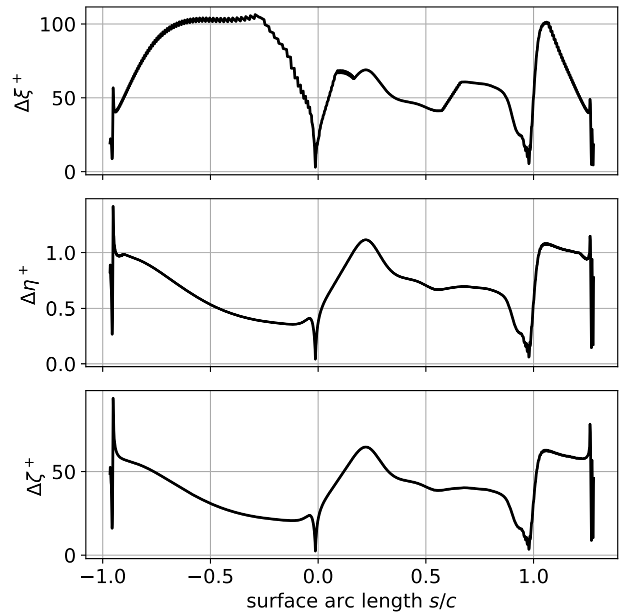

Fig. 2 Normalized non-dimensional cell spacings for the high-pressure turbine cascade VKI-LS89

3 High-pressure turbine cascade VKI-LS89

We simulate the flow over the high-pressure turbine cascade VKI-LS89 at the transonic operating point MUR235 in accordance with the experiments by Arts *et al.* [6]. There are a number of numerical studies [5, 7, 32, 33], as well as two experimental campaigns [6, 33] that serve as references for these operating conditions.

3.1 Numerical setup. The inlet boundary is located at the measurement plane of the experiment $0.81c$ upstream of the leading edge and the outlet is extended $1.48c$ downstream from the trailing edge to allow for the vortices to decay, where $c = 0.0676\text{m}$ is the chord length of the turbine blade. A turbulent inflow condition is applied at the inlet boundary, where fluctuations are introduced through the synthetic turbulence generator method by Shur *et al.* [34] (see Matha *et al.* [35], as well as the first part of this paper series for more details) with prescribed turbulence levels of 6% and a length scale of 3.19mm [7]. The domain is extruded by 14.8% chord lengths along the spanwise direction, which was found to be sufficient to resolve the generation of turbulent spots [7]. We set the pitch- and spanwise domain faces to be periodic and use a non-reflecting condition at the outlet boundary to prevent the generation of spurious waves [36]. In accordance with the experiments [6], an isothermal no-slip condition with $T_{\text{wall}} = 301.15\text{K}$ is applied at the blade wall.

The computational grid, given in Fig. 1, consists of 516,720 hexahedral elements and has been generated using DLR's block-structured mesh generator PyMesh [37]. The domain is decomposed into 4,480 blocks based on the METIS library [38]. A uniform polynomial order is of $N = 5$ yields a 6th order accurate scheme in space and results in a total of $111.6{\times}10^6$ degrees of freedom per equation. As this resolution is on the lower end of comparable numerical studies, we consider the flow to be only marginally resolved with averaged non-dimensional cell sizes of $(\overline{\Delta\xi^+}, \overline{\Delta\eta^+}, \overline{\Delta\zeta^+}) = (67.7, 0.7, 40.5)$, as shown in Fig. 2. Note that ξ, η and ζ refer to the streamwise, wall normal and spanwise directions. The respective values are computed from the non-dimensional element size normalized by the polynomial order ($\square^+ = \square^+_e/N$). High-order schemes, however, generally allow for larger cell sizes compared to classical lower-order FV methods [39] and Alhawwary & Wang [40] hinted that LES with comparable cell spacings can still produce sensible results.

The kinetic-energy conserving two-point fluxes by Kennedy & Gruber [41] are used to eliminate polynomial aliasing errors stemming from the non-linear terms and stabilize the scheme numerically. The default modal oscillation sensor with the settings presented in [21] is applied to identify troubled elements subject to shock waves.

The operating point is iteratively determined from precursor RANS simulations and the LES is initialized with the solution of the final result. Flow statistics are taken over 10 convective time units (based on the chord length and the mean outflow velocity) after an initial transient period, where the simulation is advanced in time until the free-stream turbulence has passed the domain (which is a more conservative estimate than the transient calculated using the marginal standard error rule by Bergmann *et al.* [42] in this case). The non-dimensional time-step size of the explicit time integration scheme is $\Delta t^* = \Delta t \cdot U_{\text{out}}/c = 3.8{\times}10^{-6}$, resulting in a total of $5.5{\times}10^6$ time steps for the entire LES, including the initial transient.

A summary of the simulation parameters is given in Tab. 1.

3.2 Results.

3.2.1 Shock indicator. The HPT simulation presented in this work was conducted with the default sensor settings proposed by Hennemann *et al.* [21]. The shock indicator function is visualized in Fig. 3, where the element-wise constant blending weight α is plotted together with contours of numerical schlieren $\|\nabla\rho\|_2$. The density and the blending weight are also shown along two probes across the shock (indicated by blue, dashed lines). While the FV-subcell shock capturing scheme stabilizes the solution numerically by reducing high-frequency polynomial oscillations, the modal sensor is configured to only detect the strongest oscillations (right subplot), which can leave some spurious oscillations near the discontinuity (left subplot), if their modal energy is not high enough to require larger blending weights. Increasing the sensitivity of the sensor, however, would result in higher amounts of the low-order FV in parts of the domain not subject to shock waves and an overly diffusive solution, as we discuss later in section 4.2.1, where we also propose an adaptation to the sensor.

Table 1 Overview of simulation parameters for the VKI-LS89 turbine cascade

Shock indicator	$\mathrm{Re_{out}}$ $/10^6$	$\mathrm{Ma_{out}}$	Tu_{in} / %	N	nDoF $/10^6$	nMPI	CPUh $/t_c$	$\overline{\Delta\xi^+}$	$\overline{\Delta\eta^+}$	$\overline{\Delta\zeta^+}$	$\Delta t/t_c$ $\times 10^6$	t_{avg}/t_c
modal	1.13	0.91	6	5	111.6	4,480	146,137	67.7	0.7	40.5	3.8	10.0

nDoF = number of degrees of freedom; nMPI = number of MPI ranks; $t_c = c/U_{\mathrm{out}}$; $\overline{\square^+} = \frac{1}{s}\int_0^s \square^+(\hat{s})\mathrm{d}\hat{s}$.

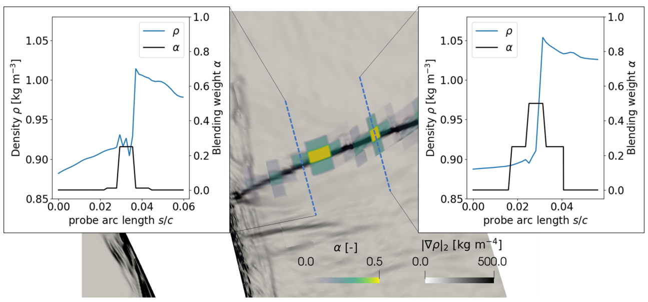

Fig. 3 Contours: numerical schlieren overlayed by the FV blending weight α. Density and blending weights plotted along to probes (blue dashed lines) given as detail plots.

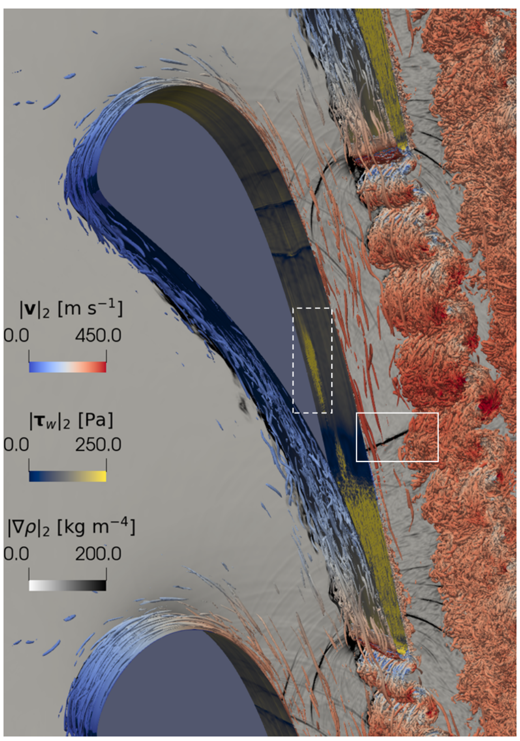

Fig. 4 Iso-surfaces of the Q-criterion colored by the local velocity magnitude and contours of numerical schlieren $\|\nabla\rho\|_2$. Blade surface colored by wall shear stress. Solid box: shock location. Dashed box: turbulent spot.

3.2.2 Flow field analysis. We visualize the instantaneous flow field in Fig. 4, where iso-surfaces of $Q \equiv (\|\mathbf{\Omega}\|^2 - \|\mathbf{S}\|^2)/2$ [43] highlight the vortical structures, contours of the density gradient $\|\nabla\rho\|_2$ indicate the compression waves and shocks, and the blade surface is colored by the wall shear stress $\|\tau_w\|_2$. Small-scale vortices from the turbulent inflow boundary are stretched and elongated along the streamwise direction as the flow accelerates through the passage and becomes locally supersonic. A normal shock wave on the suction side (solid box in Fig. 4, detail plot of the isentropic Mach number in Fig. 5) decelerates the flow again to subsonic levels and, induced by the adverse pressure gradient, forces the flow to separate (as indicated by a region of low wall shear stress beneath the shock) forming an intermittent separation bubble. Behind the shock, the flow reattaches and the boundary layer becomes fully turbulent until it sheds off at the trailing edge into a vortex street. Acoustic waves generated by the shedding of von-Karman vortices travel upstream within the subsonic flow region and merge with the standing shock, as well as impinge on the suction side of the neighboring blade row and leave a distinct footprint in the wall shear stress. As the shear stress is locally reduced by the force of the adverse pressure gradient, it forms a set of spanwise bands in the blade surface contours in Fig. 4. In addition to the disturbances from the impinging acoustic waves, the boundary layer is further destabilized by turbulent free-stream structures entering the boundary layer and intermittently causing transition of the flow which results in the formation of turbulent spots (dashed box in Fig. 4). We attribute the occurrence of these turbulent spots, despite the coarse spatial resolution, to the capability of higher-order methods to efficiently discretize the domain with low diffusion errors. Following the analysis by Dupuy *et al.* [7], the forcing through the acoustic waves is, however, not the driving mechanism behind the turbulent spot production, which they mainly attribute to the interaction of the vortical structures from the free-stream turbulence with the boundary layer. These patches of turbulence, as highlighted in Fig. 4, travel downstream and feed momentum into the separating boundary layer, thereby impeding the establishment of a permanent separation bubble (as it was observed for case with laminar inflow [25]).

As heat transfer is of great relevance for high-pressure turbine blade applications, we compare the heat transfer coefficient h of the present LES with the experimental studies by Arts *et al.* [6] (MUR235) and Cação Ferreira [33] (TUR87), as well as the LES by Segui *et al.* [5] and Dupuy *et al.* [7] in Fig. 6. Note that while the TUR87 and MUR235 were conducted at the same operating conditions despite minor differences at the outlet measurement plane, the cause for the deviation in the heat transfer coefficient remain unknown to the present authors' best knowledge. In the figure, the solid line shows the spanwise and time-averaged coefficient and the lighter, thinner lines indicate instantaneous (but spanwise-averaged) values. Error bars indicate the spanwise-averaged 68% confidence interval of the mean value. The temporal mean of the LES slightly underestimates the experimental data by Arts *et al.* [6] on the pressure side ($s/c < 0$), but matches the experiments on suction side well until $s/c \approx 0.4$ and again at the shock location ($s/c \approx 1.0$). In the region $0.4 < s < 1.0$, the impinging acoustic waves and the intermittent passing of turbulent spots cause strong fluctuations of h and the results diverge, with the LES following the experiments by Cação Ferreira [33] more closely. The same trend has also been observed by Dupuy *et al.* [7], who related the absence of the suction side plateau, as seen in [6], to a lower rate

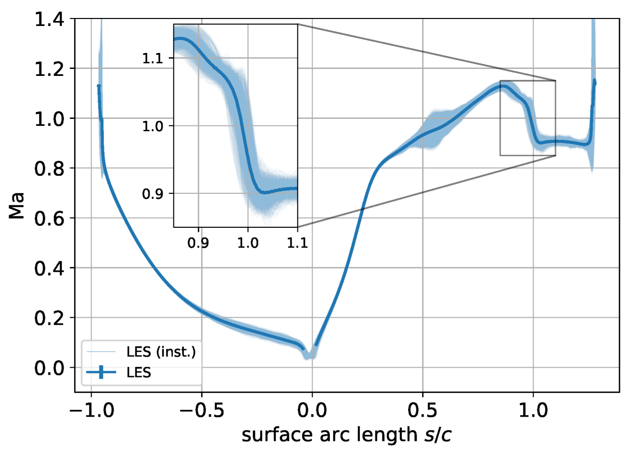

Fig. 5 Isentropic Mach number. Instantaneous, spanwise-averaged values given in light blue, time- and spanwise-averaged values in dark blue. Error bars (not visible) indicate 68% confidence interval.

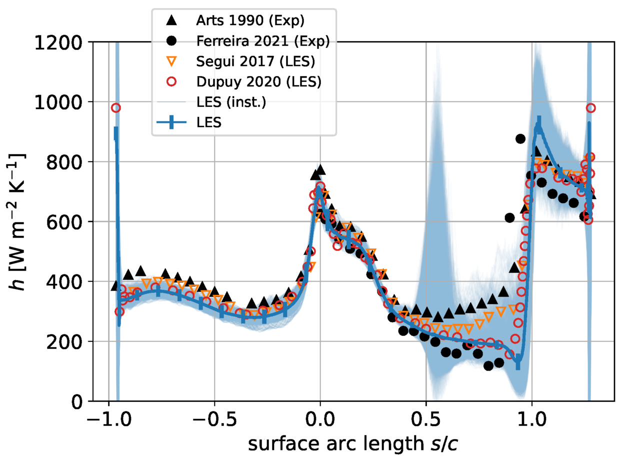

Fig. 6 Heat transfer coefficient of the current simulation in blue, experimental references in black, and numerical references in orange and red.

of turbulent spot production. While insufficient resolution could be at fault, as hinted by Segui *et al.* [5], it does not explain the mismatch in the experimental campaigns and underlines sensitive nature of the boundary layer transition of the VKI-LS89, with a reliable reference still missing.

We analyze the intermittency of the turbulent spots, the separation bubble and the shock location though the space-time diagrams in Fig. 7, which shows contours of the heat transfer coefficient (7A) and skin friction coefficient (7B) on the suction side over time. The coefficients are averaged along the span at each evaluated time step and the time on the ordinate is normalized by the reference time $t_{\mathrm{ref}} = c/U_{\mathrm{out}}$. In both plots, the shock position is indicated as iso-$\mathrm{Ma}_{\mathrm{is}}$ line (solid) and shows the location on the blade surface where $\mathrm{Ma}_{\mathrm{is}} = 1$ when going from supersonic to subsonic flow. Furthermore, the zero skin friction location (spanwise-averaged) is added in Fig. 7B to provide an estimate of the intermittent separation bubble size.

The spatiotemporal fields are characterized by a high-frequency wave-like pattern in the region $0.4 < s/c < 0.6$ and infrequent, elongated streaks of large h or C_f values between $s/c = 0.6$ and the shock location at $s/c \approx 1$, after which the coefficients abruptly increase. The high-frequency pattern at mid-chord is the surface footprint of the impinging acoustic waves from the neighboring trailing edge shedding (see the discussion relating Fig. 4 and Fig. 6 above) and reoccurs at $s/c > 1.25$. The intermittent turbulent spots, which are characterized by the streaks of large h and C_f, appear to originate at different streamwise locations, but not upstream of the wave-impingement location. The interaction of the turbulent spots with the separation bubble and the shock foot is highlighted in the space-time diagram of C_f in Fig. 7B, which shows the temporary collapse of the recirculating flow region (red) upon the passing of a turbulent spot and is consistent with [7].

While the present, marginally resolved LES of the VKI-LS89 shows that the physical phenomena observed in other studies are also captured here, the authors suggest that an increase in spatial resolution could improve the match with other reference solutions in the future.

4 DLR's compressor cascade

In this section, we present LES results from the flow over a compressor cascade at transonic operating condition. Measurement of the cascade have been conducted previously at DLR's Transonic Cascade Wind Tunnel by Klinner *et al.* [26].

4.1 Numerical setup. We simulate the flow at transonic condition aiming to match the experiments by Klinner *et al.* [26] for the off-design operating point with $\mathrm{Ma}_{\mathrm{in}} = 1.05$, $\mathrm{Re}_{\mathrm{in}} = 1.4{\times}10^6$ and $\beta_{\mathrm{in}} = 150.6°$, where the subscript *in* refers to a measurement plane located half a pitch upstream of the leading edge. The geometric dimensions of the setup are described by the pitch $t = 0.0495$m, the chord length $c = 0.07$m and the stagger angle $\beta_{\mathrm{st}} = 139.9°$. The inlet and outlet boundaries are located one pitch length upstream of the leading edge and 1.14 pitch lengths downstream from the trailing edge, respectively, with non-reflecting boundary conditions (Unsteady1DCharacteristics) reducing spurious waves at both domain faces (see [36] for a discussion on non-reflecting boudnary conditions). The blade is extruded by 5% chord length and periodic boundary conditions are set along the spanwise and pitchwise direction. To enable a more regular distribution of the blending weight across the shock than it was found in the high pressure turbine case discussed above, smaller elements with a lower polynomial order of $N = 3$ (4th order accuracy in space) are applied throughout the domain. The computational grid has been generated with the Gmsh package [44] and contains 2,276,829 hexahedral elements with a local refinement around the shock (see Fig. 8), amounting to a total of $145.7{\times}10^6$ degrees of freedom per equation. The domain is decomposed into 4,096 blocks based on the METIS library [38]. The mean non-dimensional cell-spacings are given in Fig. 9 for the streamwise (ξ), wall-normal (η) and spanwise (ζ) coordinates. The values are normalized by the polynomial order N to aid the comparability to FV simulations. The non-dimensional time-step size of the explicit time integration scheme is $\Delta t^* = \Delta t \cdot U_{\mathrm{in}}/c = 7.0{\times}10^{-6}$, resulting in a total of $8.6{\times}10^6$ time steps for the simulation.

Numerical errors arising from polynomial aliasing of the non-linear terms are canceled through the application of the entropy-conserving split-form variant by Chandrashekar [45] together with the corresponding Riemann solver. In this case, two indicator functions have been applied to identify troubled elements subject to shock waves: the modal energy sensor (Eq. (3)) and the feature-based dilatation-vorticity sensor (Eq. (6)), both with linear mapping of the blending weight. The time and space relaxation factors of the sensor are both set to 0.7, in accordance with [23].

Preliminary RANS simulations were conducted to iterate the operating conditions such that the Mach and Reynolds number, as well as the inflow angle, match the values at the inflow measurement plane (indicated in blue, Fig. 8) in the experiment by Klinner *et al.* [26]. No inflow turbulence or correction for streamline contraction is prescribed, as the experiments report free-stream

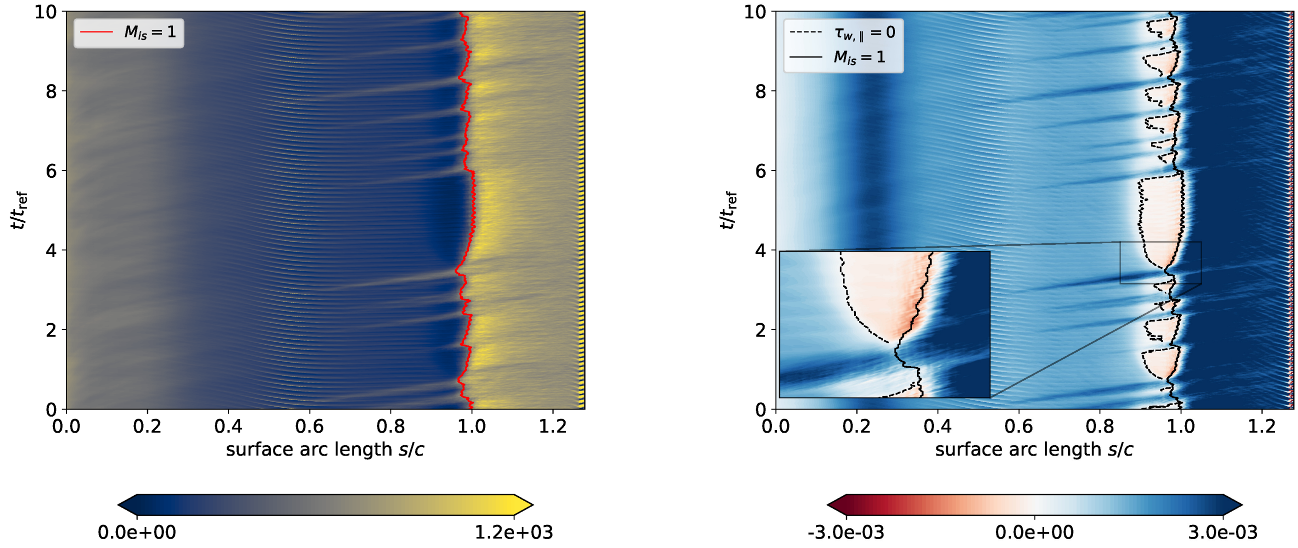

A HEAT TRANSFER COEFFICIENT

B SKIN FRICTION COEFFICIENT

Fig. 7 Space-time diagrams of the heat transfer coefficient *h* (a) and the skin friction coefficient (b). Iso-line of isentropic Mach number as red (a) and solid black (b). Spanwise-averaged zero-skin friction indicated by dashed line in (b).

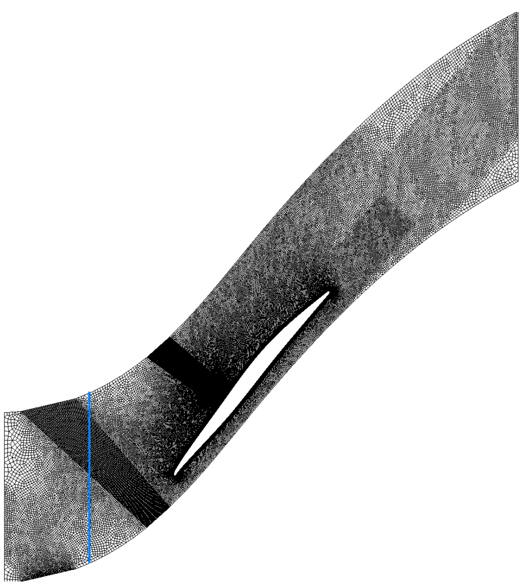

Fig. 8 Computational grid for the compressor cascade. Only elements without interior collocation points shown. Inlet measurement plane indicated in blue.

turbulence levels below 1% and an axial velocity density ratio of approximately unity [26]. The RANS results are used as initial condition for the LES, which is first run for several convective time units to get past an initial transient period, determined by the marginal standard error rule [42], and then continued to run for 20 convective time units for the acquisition of flow statistics. During the transient period, a slow drift of the shock leads to a gradual increase in the Mach number from the steady state result at the inflow measurement plane that levels out at $\mathrm{Ma_{in}} = 1.1$. The two shock sensors are evaluated and compared in the initial phase of the simulation, (see section 4.2.1), while the discussion of the flow field is based on the converged, long-running computation with the feature-based sensor (section 4.2.2).

An overview of the simulation parameters is given in Tab. 2.

4.2 Results. In the following sections, we first analyze the impact of the shock indicator choice on the flow over the transonic compressor cascade. The flow field and shock dynamics are then analyzed in more detail based on the feature-based shock sensor.

4.2.1 Comparison of shock indicator functions. To adequately resolve the shock, the computational grid is strongly refined around the assumed shock location (Fig. 8). The solution, however, is found to be highly sensitive to the choice of indicator function and the recommended settings [21] used for the simulation of the turbine cascade result in strong variations of the shock indicator. Such jumps in the accuracy of discretization can generate spurious flow gradients and structures - in particular in regions where the mesh is not aligned with the shock front.

A comparison of the default modal sensor, an adjusted modal sensor with linear mapping and the feature-based indicator is given in Fig. 10, where contours of the element-constant blending weight α and numerical schlieren $\|\nabla\rho\|_2$ are shown in the vicinity of the shock. While the small element sizes used in this case result in a more regular distribution of the blending weight across the shock than it is shown in Fig. 3, the default modal sensor fails to consistently add FV blending along the discontinuity and spurious polynomial oscillations occur at several locations. An increased sensitivity of the sensor alleviates the issue with the best results being achieved by using the linear mapping function Eq. (5) instead

Table 2 Overview of simulation parameters for the compressor cascade

Shock indicator	$\mathrm{Re}_{\mathrm{in}}$ $/10^6$	$\mathrm{Ma}_{\mathrm{in}}$	Tu_{in} / %	N	nDoF $/10^6$	nMPI	CPUh $/t_c$	$\overline{\Delta\xi^+}$	$\overline{\Delta\eta^+}$	$\overline{\Delta\zeta^+}$	$\Delta t/t_c$ $\times 10^6$	t_{avg}/t_c
feature	1.4	1.06	0	3	145.7	4,096	102,616	39.2	0.9	22.0	7.0	12.0
modal	1.4	1.06	0	3	145.7	4,096	107,013	32.5	0.8	18.6	7.0	12.0
feature*	1.4	1.10	0	3	145.7	4,096	102,616	33.8	0.8	19.2	7.0	20.0

nDoF = number of degrees of freedom; nMPI = number of MPI ranks; $t_c = c/U_{\mathrm{in}}$; $\overline{\square^+} = \frac{1}{s}\int_0^s \square^+(\hat{s})\mathrm{d}\hat{s}$, * = converged.

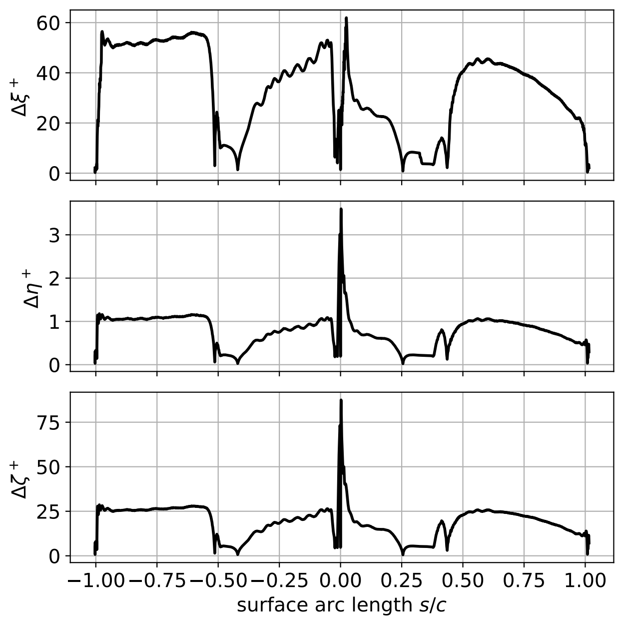

Fig. 9 Normalized non-dimensional cell spacings for the compressor cascade (feature-based indicator)

of the non-linear one (Eq. (4)), together with a lower threshold value of $\mathbb{T} = 0.0005$. The high sensitivity, however, leads to a larger amount of FV blending in elements subject to turbulence where the solution is not fully resolved (see Fig. 10B). As a result, numerical dissipation is added in addition to the Riemann solver which leads to larger-scale flow structures and damping of turbulent fluctuations. The most consistent results for shock identification over the compressor cascade are achieved by applying the feature-based shock indicator (Eq. (6)). As shown in Fig. 10C, the shock is correctly identified with higher values of α only being added outside the boundary layer, resulting in an oscillation-free shock wave.

The effect of the shock sensors on the turbulent fluctuations is evaluated in Fig. 11A, where we plot Welch's power spectral density (PSD) estimate of the wall-parallel velocity component $u_{\parallel}$ at mid-chord within the boundary layer for both sensors. The fluctuating turbulent energy of the simulation with the modal sensor is distinctly reduced over the feature-based indicator and does not show the dominant peak at 3.9 kHz. Similarly, we evaluate the shock movement by computing the PSD of the spatio-temporal oscillations of the isentropic surface Mach iso-line $x_{\mathrm{Ma}} = x|_{\mathrm{Ma_{is}}=1}$ (Fig. 11B). The figure shows that the energy content of the shock motion is only marginally impacted as both simulations feature a similar trend of the PSD with the shocks oscillating around $0.35c \pm 0.016c$ (feature) and $0.359c \pm 0.02c$ (modal). The added dissipation of the simulations with modal sensor also results in a decrease of the skin friction coefficient, which in turn leads to lower values for the non-dimensional cell sizes (see Tab. 2).

For the following discussion of the flow field, only the results of the converged simulation with the feature-based sensor are considered.

4.2.2 Flow field analysis. A snapshot of the instantaneous flow field is given in Fig. 12, with iso-surface of Q (colored by the velocity magnitude $\|\mathbf{v}\|_2$) showing the vortical structures, contours of the density gradient $\|\nabla\rho\|_2$ indicating compression and expansion waves and the blade is colored by the wall shear stress. The flow is characterized by an expansion fan on the suction side at the blade's leading edge and a normal shock wave at mid-chord that extends as a bow shock to the next blade row in pitchwise direction. Because no turbulent fluctuations are initialized at the inlet, the flow remains laminar on the suction side until it transitions to turbulence beneath the shock. Upstream of the normal shock, the thickening of the boundary layer is accompanied by a weak, oblique compression wave that connects from the boundary layer at approximately 20% chord length to the normal shock and causes the flow to separate (indicated by the zero wall shear stress contour line in white in Fig. 12) driven by the adverse pressure gradient across the wave. The separated shear layer becomes unstable and subject to Kelvin-Helmholtz waves that develop into spanwise vortices and are visible by the iso-surfaces of Q. The flow fully transitions to turbulence beneath the λ foot of the normal shock, reattaches and forms a turbulent boundary layer that sheds off at the trailing edge.

The boundary layer separation and reattachment points are visualized in more detail by the skin friction coefficient in Fig. 13, where, again, the spanwise and time-averaged coefficients are shown by solid and dashed lines for the suction and pressure surface respectively and the lighter, thinner lines indicate instantaneous (but spanwise-averaged) values. Note that the abscissa x_c refers to a coordinate in the direction of the blade's chord. On the pressure side, the downward curve of the blade nose forces the boundary layer to separate and reattach within 3% from the leading edge (see detail plot of C_f in Fig. 13), resulting in a short separation bubble. A second bubble forms further downstream and transitions the flow to a turbulent boundary layer.

To evaluate the accuracy of the results, we compare the LES with the isentropic surface Mach number $\mathrm{Ma_{is}}$ from the data obtained in the experiments by Klinner *et al.* [26] in Fig. 14. Again, the 68% confidence intervals are added, but remain hidden as the pressure distribution is near-steady in time. The plot shows that the LES is in excellent agreement with the values measured in the experiments on the pressure side (PS, dashed line), while deviations are more significant on the suction side (SS, solid line). Although the LES is able to capture the shape of $\mathrm{Ma_{is}}$ with the two plateaus upstream of the shock, its values are offset by $\mathrm{Ma_{is,LES}} - \mathrm{Ma_{is,exp}} \approx 0.03$ in the the region $0 < x_c/c < 0.3$. In the experiments, low-frequency shock oscillations over a range of ±4% chord length and a frequency of 1.7kHz were observed and are the reason for the smooth $\mathrm{Ma_{is}}$ decrease over the shock. The steeper gradient shown by the time-averaged LES results therefore suggests, that this low-frequency buffeting is not fully resolved. Behind the shock, experiments and LES converge again more closely. The near-constant offset in $\mathrm{Ma_{is}}$ upstream of the shock at mid-chord and the higher Mach number at the upstream measurement plane indicate that the operating conditions of the LES and the experiments deviate to some extent. For a more detailed discussion of shock oscillations, we refer to Hergt

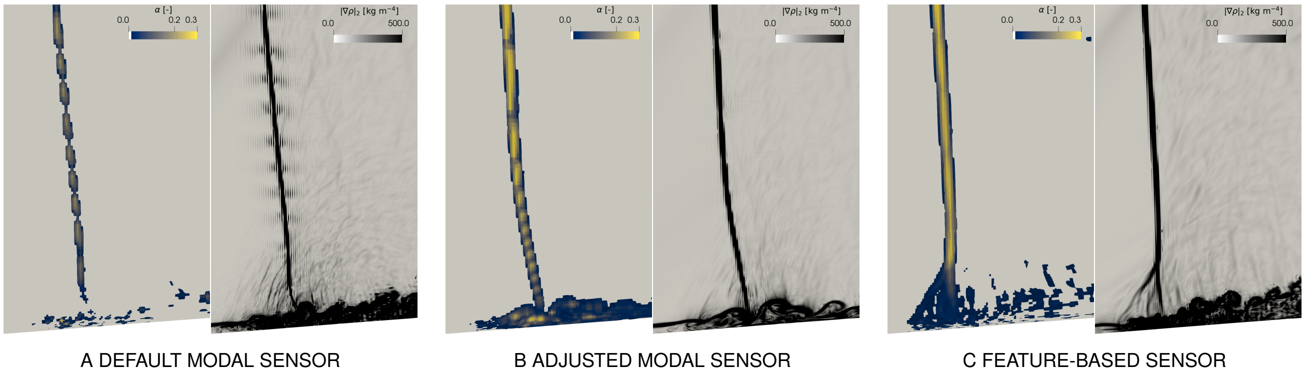

Fig. 10 Contours of the FV blending weight α and the density gradient magnitude $\|\nabla\rho\|_2$ for the default modal shock sensor (a), the adjusted modal sensor (b) and the feature-based shock sensor (c).

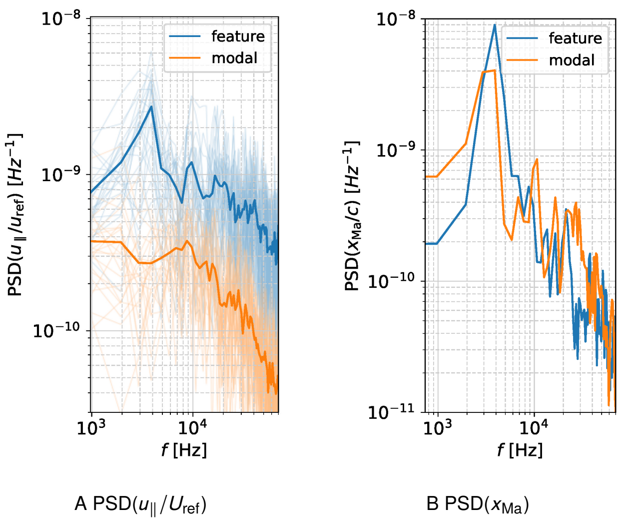

Fig. 11 (a) Power spectral density of the wall-parallel velocity sampled at mid-chord 0.05c from the wall. Spanwise averaged solution indicated by solid lines. (b) Power spectral density of the surface shock location x_{Ma}.

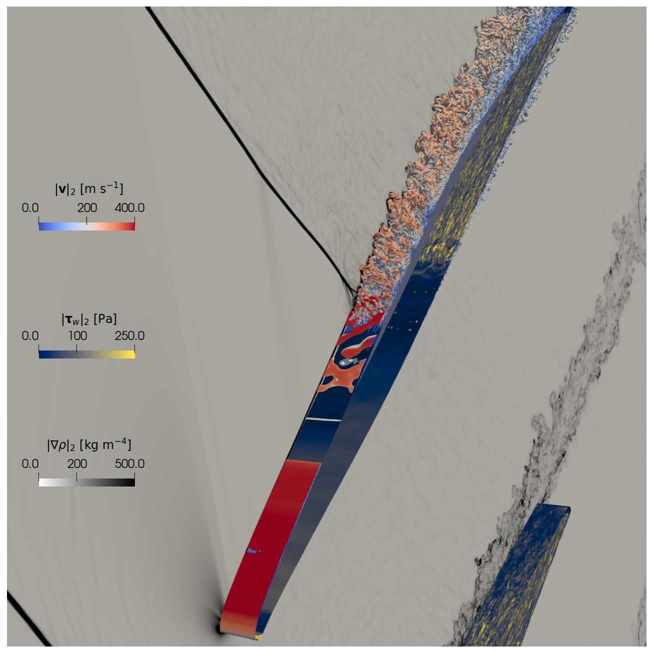

Fig. 12 Iso-surfaces of Q colored by the local velocity magnitude and contours of numerical schlieren $\|\nabla\rho\|_2$. Blade surface colored by wall shear stress.

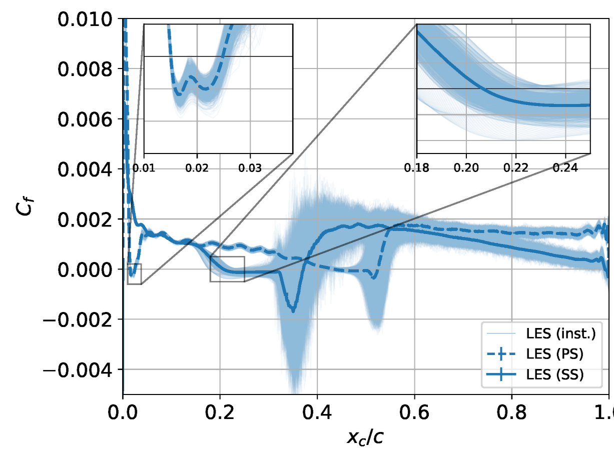

Fig. 13 Skin friction coefficient. Instantaneous, spanwise-averaged values given in light blue, time- and spanwise-averaged values in dark blue.

et al. [46].

The oscillations of the shock and the separation bubble are analyzed in more detail based on the space-time diagram of the skin friction coefficient in Fig. 15, where, again, the solution is averaged over the span at each probed time step. The separation location is indicated by the dashed iso-line of $\tau_{w,\parallel}=0$ (termed x_τ hereinafter) and the shock location is indicated by the solid iso-line of $\mathrm{Ma}_{\mathrm{is}}=1$, termed x_{Ma}. A frequency analysis based on Welch's power spectral density estimate of $x_{\mathrm{Ma}}(t)$ and $x_\tau(t)$ is given in Fig. 16, which shows that both the shock and the separation point are in a locked oscillation mode at a frequency between 2.9kHz and 3.9kHz. Analogous to the turbine case, the movement of the shock and the separation point are dependent, such that the upstream movement of the separation point increases the flow displacement at the shock location and causes it to move downstream until the growth of instabilities collapse the bubble and the process starts over. Similar observations have been made by Bode *et al.* [10] for the flow over a transonic compressor blade with inlet turbulence. The shock location and its oscillation amplitude on the surface is $x_{\mathrm{Ma}}/c=0.367\pm0.017$, which is lower than in the experiments but occurring at a higher frequency and hence assumed to be a different mechanism than the low-frequency buffeting.

While the separation bubble movement dominates the vortex dynamics on the blade, Fig. 17 shows that the dominant wake mode

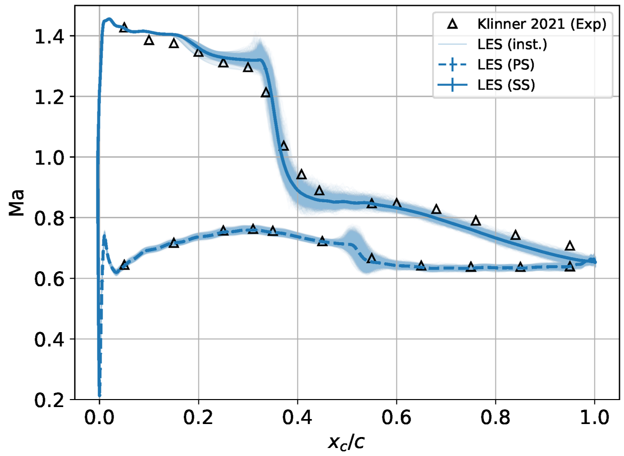

Fig. 14 Isentropic Mach number. Instantaneous, spanwise-averaged values of the LES given in light blue, time- and spanwise-averaged values in dark blue. Experimental values by Klinner *et al.* [26] in black.

occurs at a frequency of 12.6 kHz. In the figure, the PSD (Welch's approximation) of the static pressure is evaluated at a measurement plane half a pitch downstream of the trailing edge and the results are averaged over all probes along the pitch and the span with the light blue curves indicating the PSD of the single probes. The shock oscillation frequency shows as the second dominant peak in the graph (3.9 kHz), but is slightly lower than the main shedding mode. Only a minor peak at the shedding mode of 12.6 kHz is visible in the PSD of the shock movement such that the feedback mechanism of wake to shock does not appear to be the main driver of the shock oscillations here.

5 Conclusion

In the second part of this paper series, we have analyzed the flow over two transonic cascades at high Reynolds numbers with implicit LES based on the discontinuous Galerkin spectral element method and subcell-FV shock capturing: the high-pressure turbine VKI-LS89 and a compressor cascade measured at DLR [26]. Although the flow over the VKI-LS89 is only marginally resolved, physical phenomena such as the production of turbulent spots are captured. The default sensor settings [21] are shown to yield a numerically stable simulation, but admit some local spurious oscillations. For the LES over a transonic compressor cascade, we have demonstrated that a shock sensor based on flow features (dilatation-vorticity) identifies troubled elements more consistently than modal energy sensors, which were either overly dissipative in marginally resolved vortical flow regions or not able to capture the shock wave correctly. While the LES matches the isentropic Mach number on the pressure side with experiments well, only the high-frequency shock oscillations of the separation bubble shedding are resolved and not the low-frequency buffeting observed in the experiment. Differences in the operating conditions of the LES and the experiment are assumed to be at fault here, as the upstream flow condition deviates from the reported experimental values, despite closely matching the shock location.

While the simulation of transonic flows remains challenging and is still an active area of research, we have shown that TRACE-DG is capable of such computations in the context of the numerical test rig.

Acknowledgments

The authors thank Andrés Rueda-Ramírez for the discussion and his insight on the shock-capturing method.

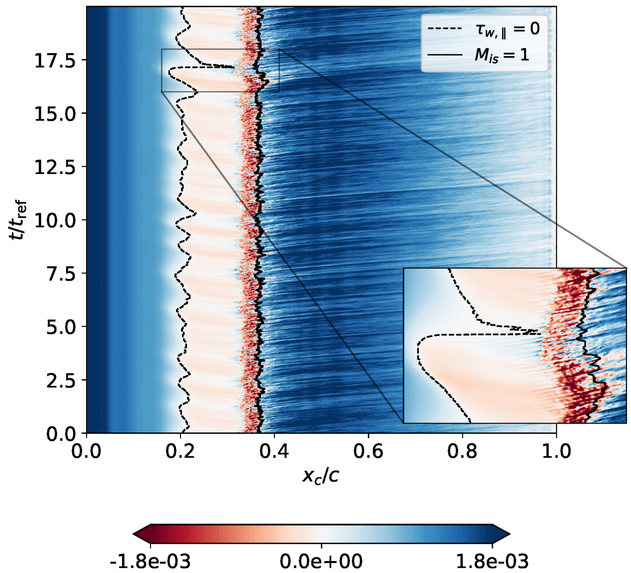

Fig. 15 Space-time diagram of the skin friction coefficient.

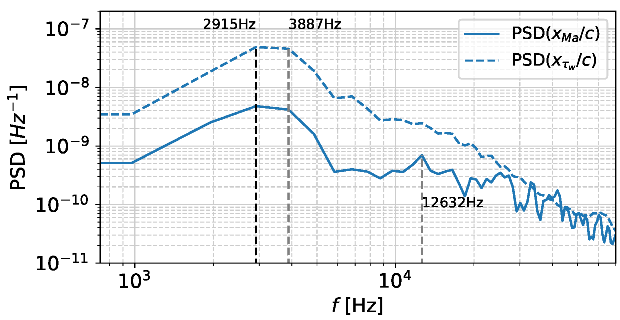

Fig. 16 Power spectral density of the surface shock location x_{Ma} and separation location x_τ.

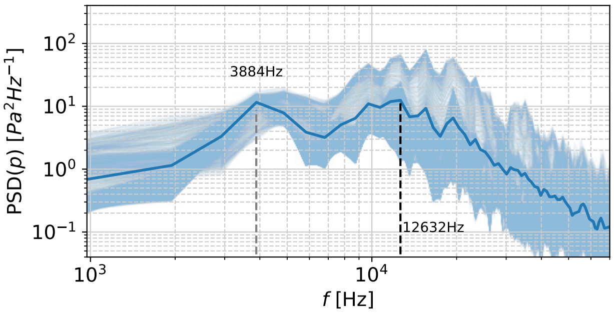

Fig. 17 Power spectral density of the pressure averaged over a 2D plane located half a pitch length downstream of the trailing edge.

Nomenclature

Roman letters

a = speed of sound [m s^{-1}]
c = chord length [m]
C_f = skin friction coefficient
E = specific total energy [m^2 s^{-2}]
$\mathbb{E}$ = energy indicator
f = frequency [s^{-1}]
$\tilde{\mathbf{F}}^*$ = interface fluxes
h = heat transfer coefficient [W m^{-2} K^{-1}]
h_β = element size along density gradient
J_i = Jacobian of coordinate transformation
m_j = modal coefficients
$\mathbf{M}_h$ = tensor of metric terms
N = polynomial order
p = pressure [Pa]
$\mathbf{q}$ = vector of conserved variables, $[\rho, \rho u, \rho v, \rho w, \rho E]^\mathrm{T}$
Q = Q-criterion [s^{-2}]
$\mathbf{R}$ = residual vector
$\mathbb{S}$ = shock sensor
s = surface arc length
s_θ = dilatation sensor
s_ω = vorticity sensor
$\mathbf{S}$ = strain rate tensor
t = pitch length [m]
t = time [s]
$\mathbb{T}$ = indicator threshold
Tu = turbulence intensity
$\mathbf{v}$ = vector of Cartesian velocity components, $[u, v, w]^\mathrm{T}$
u, v, w = Cartesian velocity components [m s^{-1}]
w_i = quadrature weight

Greek letters

α = finite-volume blending weight
β = inlet flow angle
γ = heat capacity ratio
ε = small, positive number $\ll 1$
ρ = density [kg m^{-3}]
ν = kinematic viscosity [m^2 s^{-1}]
ξ, η, ζ = streamwise, wall-normal, spanwise coordinates
$\mathbf{\Omega}$ = vorticity tensor

Dimensionless groups

Re = Reynolds number, cU_∞/ν
Ma = Mach number, $\|\mathbf{v}\|_2/a$

Superscripts and subscripts

avg = averaging interval
c = convective time unit
DG = discontinuous Galerkin
FV = finite volume
in = inflow
is = isentropic
out = outflow
ref = reference
sonic = sonic conditions
$*$ = non-dimensional
$+$ = wall units
$\|$ = streamwise direction

References

[1] Sandberg, R. D. and Michelassi, V., 2019, "The Current State of High-Fidelity Simulations for Main Gas Path Turbomachinery Components and Their Industrial Impact," Flow, Turbulence and Combustion, **102**(4), pp. 797–848.

[2] Wheeler, A. P. S., Sandberg, R. D., Sandham, N. D., Pichler, R., Michelassi, V., and Laskowski, G., 2016, "Direct Numerical Simulations of a High-Pressure Turbine Vane," Journal of Turbomachinery, **138**(7).

[3] Pichler, R., Sandberg, R. D., Laskowski, G., and Michelassi, V., 2017, "High-Fidelity Simulations of a Linear HPT Vane Cascade Subject to Varying Inlet Turbulence," *Volume 2A: Turbomachinery*, American Society of Mechanical Engineers, doi: 10.1115/gt2017-63079.

[4] Garai, A., Diosady, L. T., Murman, S. M., and Madavan, N. K., 2017, "Scale-Resolving Simulations of Bypass Transition in a High-Pressure Turbine Cascade Using a Spectral-Element Discontinuous-Galerkin Method," *Volume 2B: Turbomachinery*, American Society of Mechanical Engineers, doi: 10.1115/gt2017-64697.

[5] Seguí, L. M., Gicquel, L. Y. M., Duchaine, F., and de Laborderie, J., 2018, "Importance of Boundary Layer Transition in a High-Pressure Turbine Cascade Using LES," *Volume 2C: Turbomachinery*, American Society of Mechanical Engineers, doi: 10.1115/gt2018-75711.

[6] Arts, T., De Rouvroit, M. L., and Rutherford, A. W., 1990, "Aero-thermal investigation of a highly loaded transonic linear turbine guide vane cascade: A test case for inviscid and viscous flow computations," Von Karman Institute for Fluid Dynamics, https://resolver.tudelft.nl/uuid:1bdc512b-a625-4607-a339-3cc9b371215e

[7] Dupuy, D., Gicquel, L., Odier, N., Duchaine, F., and Arts, T., 2020, "Analysis of the effect of intermittency in a high-pressure turbine blade," Physics of Fluids, **32**(9), p. 095101.

[8] Zhao, Y. and Sandberg, R. D., 2020, "Bypass transition in boundary layers subject to strong pressure gradient and curvature effects," Journal of Fluid Mechanics, **888**.

[9] Zhao, Y. and Sandberg, R. D., 2021, "High-Fidelity Simulations of a High-Pressure Turbine Vane Subject to Large Disturbances: Effect of Exit Mach Number on Losses," Journal of Turbomachinery, **143**(9).

[10] Bode, C., Przytarski, P. J., Leggett, J., and Sandberg, R. D., 2022, "Highly Resolved Large-Eddy Simulations of a Transonic Compressor Stage Midspan Section Part I: Effect of Inflow Disturbances," *Volume 10D: Turbomachinery — Multidisciplinary Design Approaches, Optimization, and Uncertainty Quantification; Turbomachinery General Interest; Unsteady Flows in Turbomachinery*, American Society of Mechanical Engineers, doi: 10.1115/gt2022-81673.

[11] Wang, Z., Fidkowski, K., Abgrall, R., Bassi, F., Caraeni, D., Cary, A., Deconinck, H., Hartmann, R., Hillewaert, K., Huynh, H., Kroll, N., May, G., Persson, P.-O., van Leer, B., and Visbal, M., 2013, "High-order CFD methods: current status and perspective," International Journal for Numerical Methods in Fluids, **72**(8), pp. 811–845.

[12] Kronbichler, M. and Persson, P.-O., eds., 2021, *Efficient High-Order Discretizations for Computational Fluid Dynamics*, Springer International Publishing.

[13] Hindenlang, F. J., Gassner, G. J., and Munz, C.-D., 2014, "Improving the accuracy of discontinuous Galerkin schemes at boundary layers," International Journal for Numerical Methods in Fluids, **75**(6), pp. 385–402.

[14] Gassner, G. J., Winters, A. R., and Kopriva, D. A., 2016, "Split form nodal discontinuous Galerkin schemes with summation-by-parts property for the compressible Euler equations," Journal of Computational Physics, **327**, pp. 39–66.

[15] Winters, A. R., Moura, R. C., Mengaldo, G., Gassner, G. J., Walch, S., Peiro, J., and Sherwin, S. J., 2018, "A comparative study on polynomial dealiasing and split form discontinuous Galerkin schemes for under-resolved turbulence computations," Journal of Computational Physics, **372**, pp. 1–21.

[16] Garai, A., Diosady, L., Murman, S., and Madavan, N., 2015, "DNS of Flow in a Low-Pressure Turbine Cascade Using a Discontinuous-Galerkin Spectral-Element Method," *Volume 2B: Turbomachinery*, American Society of Mechanical Engineers, doi: 10.1115/gt2015-42773.

[17] Persson, P.-O. and Peraire, J., 2006, "Sub-Cell Shock Capturing for Discontinuous Galerkin Methods," *44th AIAA Aerospace Sciences Meeting and Exhibit*, American Institute of Aeronautics and Astronautics, doi: 10.2514/6.2006-112.

[18] Chaudhuri, A., Jacobs, G., Don, W., Abbassi, H., and Mashayek, F., 2017, "Explicit discontinuous spectral element method with entropy generation based artificial viscosity for shocked viscous flows," Journal of Computational Physics, **332**, pp. 99–117.

[19] Yu, J. and Hesthaven, J. S., 2020, "A Study of Several Artificial Viscosity Models within the Discontinuous Galerkin Framework," Communications in Computational Physics, **27**(5), pp. 1309–1343.

[20] Sonntag, M. and Munz, C.-D., 2016, “Efficient Parallelization of a Shock Capturing for Discontinuous Galerkin Methods using Finite Volume Sub-cells,” Journal of Scientific Computing, **70**(3), pp. 1262–1289.
[21] Hennemann, S., Rueda-Ramírez, A. M., Hindenlang, F. J., and Gassner, G. J., 2021, “A provably entropy stable subcell shock capturing approach for high order split form DG for the compressible Euler equations,” Journal of Computational Physics, **426**, p. 109935.
[22] Mossier, P., Beck, A., and Munz, C.-D., 2022, “A p-Adaptive Discontinuous Galerkin Method with hp-Shock Capturing,” Journal of Scientific Computing, **91**(1).
[23] Rueda-Ramírez, A. M., Pazner, W., and Gassner, G. J., 2022, “Subcell limiting strategies for discontinuous Galerkin spectral element methods,” Computers & Fluids, p. 105627.
[24] Dzanic, T. and Witherden, F., 2022, “Positivity-preserving entropy-based adaptive filtering for discontinuous spectral element methods,” Journal of Computational Physics, **468**, p. 111501.
[25] Klose, B., Morsbach, C., Bergmann, M., and Kügeler, E., 2022, “Implicit LES of the Transonic Flow Over A High-Pressure Turbine Cascade using DG Subcell Shock Capturing,” *8th European Congress on Computational Methods in Applied Sciences and Engineering*, CIMNE, doi: 10.23967/eccomas.2022.144.
[26] Klinner, J., Hergt, A., Grund, S., and Willert, C. E., 2021, “High-Speed PIV of shock boundary layer interactions in the transonic buffet flow of a compressor cascade,” Experiments in Fluids, **62**(3).
[27] Fernandez, P., Nguyen, N.-C., and Peraire, J., 2018, “A physics-based shock capturing method for large-eddy simulation,” .
[28] Kopriva, D. A., 2009, *Implementing Spectral Methods for Partial Differential Equations*, Springer Netherlands.
[29] Bassi, F. and Rebay, S., 1997, “A High-Order Accurate Discontinuous Finite Element Method for the Numerical Solution of the Compressible Navier–Stokes Equations,” Journal of Computational Physics, **131**(2), pp. 267–279.
[30] Bergmann, M., Morsbach, C., and Ashcroft, G., 2020, “Assessment of Split Form Nodal Discontinuous Galerkin Schemes for the LES of a Low Pressure Turbine Profile,” *ERCOFTAC Series*, Springer International Publishing, pp. 365–371.
[31] Bergmann, M., Gölden, R., and Morsbach, C., 2018, “Numerical investigation of split form nodal discontinuous Galerkin schemes for the implicit LES of a turbulent channel flow,” *Proceedings of the 7th European Conference on Computational Fluid Dynamics*.
[32] Morata, E. C., Gourdain, N., Duchaine, F., and Gicquel, L., 2012, “Effects of free-stream turbulence on high pressure turbine blade heat transfer predicted by structured and unstructured LES,” International Journal of Heat and Mass Transfer, **55**(21-22), pp. 5754–5768.
[33] Cação Ferreira, T. S., 2021, “Boundary layer transition and convective heat transfer of the high-pressureturbine vane LS89,” Ph.D. thesis, Universite catholique de Louvain.
[34] Shur, M. L., Spalart, P. R., Strelets, M. K., and Travin, A. K., 2014, “Synthetic Turbulence Generators for RANS-LES Interfaces in Zonal Simulations of Aerodynamic and Aeroacoustic Problems,” Flow, Turbulence and Combustion, **93**(1), pp. 63–92.
[35] Matha, M., Morsbach, C., and Bergmann, M., 2018, “A comparison of methods for introducing synthetic turbulence,” 7th European Conference on Computational Fluid Dynamics.
[36] Schlüß, D., Frey, C., and Ashcroft, G., 2016, “Consistent Non-reflecting Boundary Conditions For Both Steady And Unsteady Flow Simulations In Turbomachinery Applications,” *ECCOMAS Congress 2016 VII European Congress on Computational Methods in Applied Sciences and Engineering, Crete Island, Greece*.
[37] Weber, A. and Sauer, M., 2016, “PyMesh - Template Documentation,” German Aerospace Center (DLR), Institute of Propulsion Technology, Linder Hoehe, Cologne, Germany, techreport DLR-IB-AT-KP-2016-34.
[38] Karypis, G. and Kumar, V., 1998, “A fast and high quality multilevel scheme for partitioning irregular graphs,” SIAM JOURNAL ON SCIENTIFIC COMPUTING, **20**(1), pp. 359–392.
[39] Georgiadis, N. J., Rizzetta, D. P., and Fureby, C., 2010, “Large-Eddy Simulation: Current Capabilities, Recommended Practices, and Future Research,” AIAA Journal, **48**(8), pp. 1772–1784.
[40] Alhawwary, M. and Wang, Z., 2019, “On the mesh resolution of industrial LES based on the DNS of flow over the T106C turbine,” Advances in Aerodynamics, **1**(1).
[41] Kennedy, C. A. and Gruber, A., 2008, “Reduced aliasing formulations of the convective terms within the Navier–Stokes equations for a compressible fluid,” Journal of Computational Physics, **227**(3), pp. 1676–1700.
[42] Bergmann, M., Morsbach, C., Ashcroft, G., and Kügeler, E., 2021, “Statistical Error Estimation Methods for Engineering-Relevant Quantities From Scale-Resolving Simulations,” Journal of Turbomachinery, **144**(3).
[43] Jeong, J. and Hussain, F., 1995, “On the identification of a vortex,” Journal of Fluid Mechanics, **285**, pp. 69–94.
[44] Geuzaine, C. and Remacle, J.-F., 2009, “Gmsh: A 3-D finite element mesh generator with built-in pre- and post-processing facilities,” International Journal for Numerical Methods in Engineering, **79**(11), pp. 1309–1331.
[45] Chandrashekar, P., 2013, “Kinetic Energy Preserving and Entropy Stable Finite Volume Schemes for Compressible Euler and Navier-Stokes Equations,” Communications in Computational Physics, **14**(5), pp. 1252–1286.
[46] Hergt, A., Klose, B., Klinner, J., Bergmann, M., Lopez, E. M., Grund, S., and Morsbach, C., 2023, “Draft: On the Shock Boundary Layer Interaction in Transonic Compressor Blading,” *Proceedings of the ASME Turbo Expo 2023*.

List of Figures

List of Tables